



Hyperspectral imaging with a TWINS birefringent interferometer

A. PERRI,^{1,2,4} B. E. NOGUEIRA DE FARIA,^{3,4} D. C. TELES FERREIRA,³ D. COMELLI,¹ G. VALENTINI,¹ F. PREDÀ,^{1,2} D. POLLI,^{1,2} A. M. DE PAULA,³ G. CERULLO,^{1,2} AND C. MANZONI^{1,*}

¹IFN-CNR, Dipartimento di Fisica, Politecnico di Milano, Piazza Leonardo da Vinci 32, I-20133 Milano, Italy

²NIREOS S.R.L., Via G. Durando 39, 20158 Milano, Italy

³Departamento de Física, Universidade Federal de Minas Gerais, 31270-901 Belo Horizonte-MG, Brazil

⁴The authors contributed equally to the work

*cristian.manzoni@polimi.it

Abstract: We introduce a high-performance hyperspectral camera based on the Fourier-transform approach, where the two delayed images are generated by the Translating-Wedge-Based Identical Pulses eNcoding System (TWINS) [Opt. Lett. **37**, 3027 (2012)], a common-path birefringent interferometer that combines compactness, intrinsic interferometric delay precision, long-term stability and insensitivity to vibrations. In our imaging system, TWINS is employed as a time-scanning interferometer and generates high-contrast interferograms at the single-pixel level. The camera exhibits high throughput and provides hyperspectral images with spectral background level of -30 dB and resolution of 3 THz in the visible spectral range. We show high-quality spectral measurements of absolute reflectance, fluorescence and transmission of artistic objects with various lateral sizes.

© 2019 Optical Society of America under the terms of the [OSA Open Access Publishing Agreement](#)

1. Introduction

A great deal of physico-chemical information on objects can be obtained by measuring the spectrum of the light they emit, scatter or reflect. Spectral imaging, also known as imaging spectroscopy [1], refers to a set of methods and devices for acquiring the light spectrum for each point in the image of a scene. Among them, hyperspectral imaging (HSI) [2] acquires the full continuous spectrum of light for each point (x,y) of the scene, resulting in a three-dimensional data-cube as a function of (x,y,ω) , where ω is the frequency. Starting from the spectral information, numerical methods enable extracting quantitative parameters related to chemical and physical properties of the imaged objects [3,4]. HSI is a powerful technique for a wide range of fundamental and applied studies in fields as diverse as remote sensing [5,6], medical imaging [7], agriculture [8,9], coastal and geological prospecting [10,11], safety and security [12], archaeology [13,14] and conservation science [15]. HSI has been implemented in a wide variety of methods [1]. The most straightforward approaches are Snapshot HSI [16] which uses a mosaic of bandpass filters on the detector surface, and spectral (or staring) HSI, which uses a tunable spectral filter in front of a monochrome imaging camera [17]. However, these techniques only enable acquisition of a discrete number of bands. To measure continuous spectra, a common method is spatial scanning HSI, which combines a dispersive spectrometer with a raster-scanning approach, either in point scanning (whisk-broom) or line scanning (push-broom) modes. This technique is currently implemented in most commercial HSI systems, but the high losses imposed by the entrance slit of the spectrometer lead to long acquisition times.

An alternative HSI method combines a monochrome imaging camera with a Fourier-transform (FT) spectrometer [18]. In FT spectroscopy an optical waveform is split in two

collinear delayed replicas, whose interference pattern is measured by a detector as a function of their delay. The FT of the resulting interferogram yields the continuous-intensity spectrum of the waveform. FT spectrometers have prominent advantages over dispersive ones: (i) higher signal-to-noise ratio in a readout-noise-dominated regime (the Fellgett multiplex advantage [19]); (ii) higher throughput, due to the absence of slits (the Jacquinot étendu advantage [20]); (iii) flexible spectral resolution, which is adjusted at will by varying the maximum scan delay; (iv) possibility of parallel recording of the spectra of all pixels within a two-dimensional scene of an imaging system.

A FT-based imaging system must fulfil two key requirements: (i) the delay of the replicas must be controlled to within a fraction (1/100 or better) of the optical cycle (e.g., 0.02 fs at 600 nm); (ii) the bundle of rays that form the interferogram at a given pixel must have a high degree of coherence. This last requirement guarantees visibility of the interference fringes, which is one of the most important criteria for evaluating the performance of an interference imaging spectrometer, as it determines the quality of the retrieved spectrum of a scene, and is essential for spectroscopic analysis with high accuracy. FT-based imaging is achieved using either a static or a temporal approach. In the static scheme, the interferometer has no moving parts, and a spatial interferogram is formed along one of the dimensions of the image. The acquisition is performed by moving the object with respect to the camera [21], making this method particularly suited in production lines, in which the object to be measured is moving e.g. on a conveyor belt, or for airborne remote sensing. In the temporal approach, the interferometer is scanned in order to vary the delay of the replicas, with no need of relative movement between the object and the camera. This method is better suited for the imaging of stationary objects. FT HSI systems have been built based on Michelson or Mach-Zehnder interferometers [22]; however, since they are sensitive to vibrations, it is difficult to achieve the required interferometric stability without active stabilization or tracking. Alternatively, liquid crystal cells have been used to introduce a voltage-controlled delay between orthogonal polarizations [23–25]. In the last few years, birefringent interferometers have attracted particular attention because of their compactness and insensitivity to vibrations, due to their common-path nature. They are mostly based on Wollaston or Savart prisms [26,27], or their variants [28]; because of the arrangement of their optical axes, they are characterized by a strong chromatic lateral displacement, which reduces the visibility of the interference fringes [29].

Recently we introduced the Translating-Wedge-based Identical pulses eNcoding System (TWINS) [30,31], a common-path birefringent interferometer inspired by the Babinet–Soleil compensator, but conceived to provide retardation of hundreds of optical cycles between two orthogonal polarizations of a light beam. Thanks to the favorable arrangement of the optical axes, the light replicas in TWINS are collinear, with no lateral displacement, thus guaranteeing very high contrast of the interference fringes. In addition, as the two fields share a common optical path, their delay is adjusted with interferometric precision, with fluctuations as small as 1/360 of the optical cycle without any active stabilization or tracking [30]. The TWINS interferometer has been successfully employed as a FT spectrometer in spectral ranges from the visible [32,33] to the mid-infrared [34,35], with both coherent and incoherent light beams.

In this paper we introduce a compact, low-cost hyperspectral camera using the temporal FT approach, in which the interferometer is based on the simplified version the birefringent TWINS device [32,33]. Our approach combines the advantages of FT HSI with the robustness, accuracy and high contrast of TWINS. We demonstrate that TWINS applied to FT imaging provides a high degree of coherence at each pixel of the image. This enables HSI with short acquisition times, high spectral accuracy, and background level of only -30 dB. The simplicity of our experimental configuration combined with the high spatial and spectral quality of the data-cube promise to broaden the application fields of HSI.

2. The TWINS-based hyperspectral camera

2.1. Experimental setup

A scheme of the hyperspectral camera is shown in Fig. 1. It consists of a TWINS interferometer (P1, A, B and P2) followed by a monochrome imaging system.

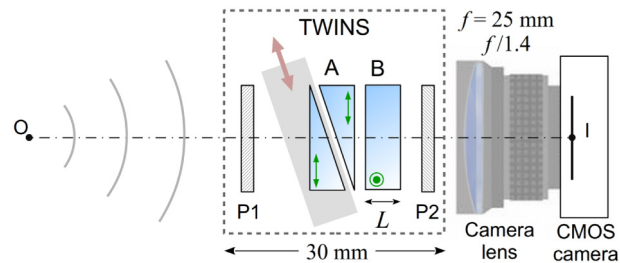


Fig. 1. Schematic setup of the hyperspectral camera. P1 and P2: wire-grid polarizers; A block: α -BBO wedges, with optical axis parallel to the plane (green double arrow); B block: α -BBO plate, with optical axis normal to the plane (green circle). The brown double arrow indicates the wedge translation direction. O: object; I: image.

A and B are birefringent blocks made of α -barium borate (α -BBO), P1 and P2 are wire-grid polarizers with extinction ratio >5000 at wavelengths from 400 nm to 2 μ m. P1 polarizes the input light at 45° with respect to the optical axes of A and B. Block B is a plate with thickness $L = 2.4$ mm and aperture diameter $D = 5$ mm; it introduces a fixed phase delay between the two orthogonal polarizations that propagate along the fast and slow axes of the material. Block A has optical axis orthogonal to the one of block B (see green arrows and circle in Fig. 1, respectively), thus applying a delay with opposite sign. The overall phase delay introduced by the TWINS ranges from positive to negative values according to the relative thickness of the two blocks. To enable fine tuning of the phase delay, block A is shaped in the form of two wedges with the same apex angle (7°), one of which is mounted on a motorized translation stage (L-402.10SD, Physik Instrumente) with maximum travel range of 13 mm. Interference between the two replicas is guaranteed by P2, which is also set at 45° with respect to the optical axes of A and B, and projects the two fields to the same polarization. The spectral resolution of the interferometer is inversely proportional to the total phase delay. For example, scanning the position of the wedges ± 1 mm around the zero path delay (ZPD) introduces a delay of ± 50 fs to the replicas of a wave at $\lambda = 600$ nm; this corresponds to spectral resolution of 15 THz (~ 18 nm). The camera lens has focal length $f = 25$ mm and maximum aperture $f/1.4$. The detector is a monochrome CMOS silicon camera with size 6.78 mm \times 5.43 mm (1/1.8" format), 1280 \times 1024 pixels, with 10-bits depth and spectral sensitivity from 400 nm to 1100 nm. The total angular field of view of the combined camera lens and detector is 15.4° (19° along the sensor diagonal).

2.2. Imaging capability of the TWINS interferometer

In the following, we will show under which conditions our TWINS birefringent interferometer enables performing FT spectral imaging. In general, an imaging system must maintain coherence (i.e., similar path delay) between the rays of the bundle that form the interferogram at a given pixel. To this aim, we will follow the pencil of rays propagating from one object point O to the detector surface of our camera, and we will calculate the relative phase they accumulate due to the interferometer.

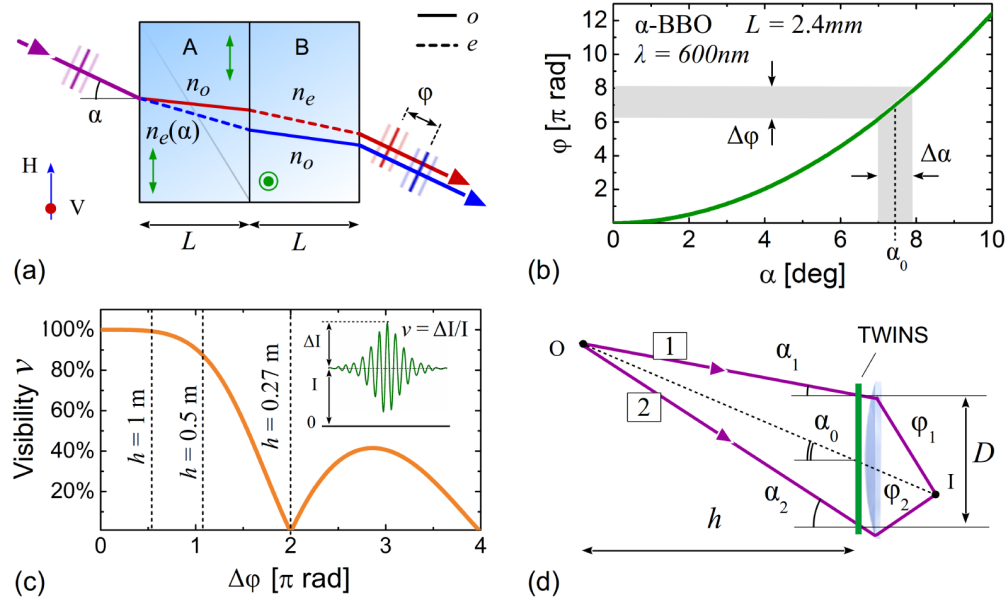


Fig. 2. (a) Top view of the optical paths and refractive indexes of the vertically-polarized (V, red) and horizontally-polarized (H, blue) components of a ray traveling in the TWINS system; dashed lines: extraordinary (e) rays; solid lines: ordinary (o) rays. Air spacing between the surfaces has been removed for simplicity. (b) Relative phase accumulated by the cross-polarized components as a function of α . (c) Visibility of the interferogram of a CW wave, as a function of the phase spread $\Delta\phi$. Vertical lines correspond to various distances h of an object at the edge of the field of view of our camera. Inset: definition of v . (d) Diagram of two marginal rays (1 and 2) propagating from the sources point O to the image point I; ϕ_1, ϕ_2 : relative phase between the vertically- and horizontally-polarized components of the field replicas.

Figure 2(a) shows the path of one generic ray impinging at angle α onto two birefringent plates with orthogonal optical axes. The plates mimic blocks A and B of the TWINS interferometer; we consider the case in which they have the same thickness L , i.e. the nominal delay T of the interferometer is set to 0. Due to birefringence, the beam splits into two orthogonally polarized replicas, which travel along different optical paths. The ordinary beams experience the same ordinary index n_o , while the extraordinary beams experience $n_e(\alpha)$ and n_e in blocks A and B respectively. As a consequence, at the output of the interferometer the horizontally-polarized component of the field (blue) is phase-shifted by ϕ with respect to the vertically-polarized one (red). The dependence of ϕ on α , calculated without loss of generality at the working conditions of our interferometer ($\lambda = 600$ nm, in α -BBO crystal with $L = 2.4$ mm), is shown in Fig. 2(b). The rays of a bundle typically impinge onto the interferometer at various angles around α_0 , with range $\Delta\alpha$; hence their phase shifts vary within $\Delta\phi$. Such a phase span leads to a reduction of the fringe visibility v at the image point. To evaluate v , let's consider the two replicas of a generic i -th ray of the bundle at frequency ω . In the frame of reference of the vertically polarized beam and in the neighborhood of $T = 0$, they can be written as:

$$E_i = A_i \cdot \{\cos[\omega t] + \cos[\omega(t - T) - \phi_i]\}. \quad (1)$$

The overlap at the image pixel I of all rays from O (see Fig. 2(d)) results in $E_i(T) = \sum_i E_i$. By taking the summation, we obtain that the resulting interferogram intensity $I = \langle E_i(T)^2 \rangle$ depends on the distribution of phase shifts ϕ_i . In the worst-case assumption that all rays have

the same amplitude A_i and their phase φ_i uniformly spans within $\Delta\varphi$, the visibility v of $\langle E_i(T)^2 \rangle$ calculated as a function of $\Delta\varphi$ is shown in Fig. 2(c).

With these general concepts, we can now estimate the fringe visibility expected from our hyperspectral camera. Figure 2(d) schematically sketches its essential optical elements, along with the path of the light from one object point O to the corresponding image point I; the object is at angle α_0 , and the incidence angles α of its pencil of rays range from α_1 to α_2 , where 1 and 2 are the marginal rays. According to Fig. 2(d), the range $\Delta\alpha$ is:

$$\Delta\alpha = |\alpha_1 - \alpha_2| \approx \arctan \frac{D/h}{1 + \tan^2 \alpha_0} < \arctan(D/h). \quad (2)$$

which is broader when the object is closer to the camera. The corresponding phase shifts range from $\varphi_1 = \varphi(\alpha_1)$ to $\varphi_2 = \varphi(\alpha_2)$.

Let's now focus on the object points with the worst fringe visibility, i.e. the ones accumulating the largest value of $\Delta\varphi$ at the image pixel. Since $\Delta\varphi$ is, to the first order, the product between $\Delta\alpha$ and the slope of the curve $\varphi(\alpha)$, larger values of $\Delta\varphi$ are obtained where the slope of the curve $\varphi(\alpha)$ is the steepest, i.e. at the edge of the field of view (see Fig. 2(b)) and for large values of $\Delta\alpha$, i.e. when the object is close to the camera lens (see Eq. (2)). In the case of our camera, an object placed at the edge of the field of view is at $\alpha_0 = 7.7^\circ$. The amplitudes of $\Delta\varphi$ and the corresponding visibility calculated for various distances h from the camera lens are shown in Fig. 2(c) as dashed vertical lines. The calculation demonstrates that the camera is expected to provide visibility larger than 85% at all pixels for objects farther than 0.5m from the camera lens. At shorter distances, the visibility slowly vanishes, especially at the edge of the field of view. The high visibility demonstrates that our scheme is well suited for FT HSI.

3. Characterization of the camera performances

The hyperspectral camera was tested for the analysis of various objects, with variable properties and lateral size. In all cases we performed single-sweep acquisitions, moving the translation stage with nominal steps of 5 μm , and took a single-exposure image at each delay. The total length of the scan was adjusted to achieve the desired spectral resolution. Note that the sampling step corresponds to a phase delay of 0.25 fs at $\lambda = 600$ nm, equivalent to 1/8 of the optical cycle; this oversampling with respect to the Nyquist limit enables improving the S/N ratio of the acquisition. To demonstrate that the TWINS interferometer is able to measure spectra with high accuracy, we imaged a test scene made of a set of calibrated spectral standards, as shown in Figs. 3(a) and 3(b): the test scene consists of 4 colored Spectralon materials (green, blue, red, yellow, G, B, R, Y), acting as calibrated diffusive reflectance standards (Labsphere Inc., North Sutton, USA), and a white Spectralon (W), with $(98.3 \pm 1.3)\%$ reflectance in the range from 300 nm to 2.5 μm (Labsphere Inc.); each of them has diameter of 1 inch. In addition, the beams of a green ($\lambda = 532$ nm) and a red diode laser ($\lambda = 635$ nm), both with bandwidth of 0.37 THz, were directed on points L1 and L2 respectively.

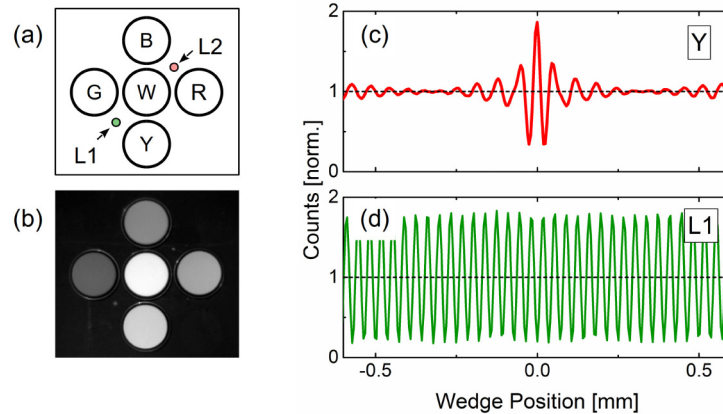


Fig. 3. (a) Geometrical arrangement and (b) intensity single-exposure image of the test object, taken at delay position of 1 mm (the complete temporal data cube as an animation is shown in the associated [Visualization 1](#)). G, B, R, Y: Spectralon diffuse color standards; W: Spectralon white standard; L1/L2: beam spots of diode lasers at $\lambda = 532$ nm/635 nm. (c) Single-scan interferogram of one image point at the surface of the Y color standard and (d) at L1.

The scene was illuminated by a broadband 150W Xenon lamp. The camera lens was set at its largest aperture and the integration time for each snapshot was only 25 ms. We scanned the position of the wedges ± 1 mm around the ZPD, corresponding to a total of 400 images. The acquisition of the data-cube, including lapse time for motor movement and data transfer, required less than 30 seconds. This acquisition time could be further reduced by optimizing the digital communication with the camera and by sampling with longer steps to reduce the number of images (eventually employing undersampling strategies). Figures 3(c) and 3(d) show a portion of the raw interferograms of two pixels, on the region of the Y colored standard and on the L1 area. The fringe visibility of the two interferograms is 86.5% and 84% respectively. The high contrast proves that, when placed before the camera lens, the TWINS interferometer provides high degree of coherence at the single-pixel level, as required by FT HSI. Note that high contrast also reduces the spectral background noise, since the contribution to the noise of the A/D conversion of the interferogram is inversely proportional to the visibility [36]. The high contrast can be further improved by closing the lens aperture, at the cost of reducing the light flux on the detector.

3.1. Frequency calibration and resolution

The narrowband green ($\lambda = 532$ nm) and red ($\lambda = 635$ nm) diode laser spots in L1 and L2 enable the spectral characterization of the camera. Figure 4(a) shows their resulting normalized spectra. From their acquisition, the following information can be obtained:

- (i) the positions of their spectral peaks enable the calibration of the frequency axis of the FT spectrometer [30,32];
- (ii) their bandwidth provides the spectral resolution of the interferometer which, for ± 5 -mm scan, is 3THz (~ 4 nm at $\lambda = 635$ nm), corresponding to 1/150 of the spectral range of the camera. For this high-resolution measurement, we acquired 1000 images with nominal sampling steps of 10 μ m, and the acquisition required 95 seconds;
- (iii) the interferogram (see Fig. 3(d) for L1) allows retrieving with sub-cycle precision the true delay of the interferometer during the scan. The detailed description of the technique and the measured deviation from the expected wedge position are reported in the Appendix section. By using the measured positioning for the FT calculation, the spectral background level is 30dB lower than the peak, as shown in the inset of Fig. 4(a). Note that this self-calibration procedure, which simply requires shining laser light in a small

part of the scene (e.g. L1 and/or L2), is an effective alternative to internal encoders or feedback systems.

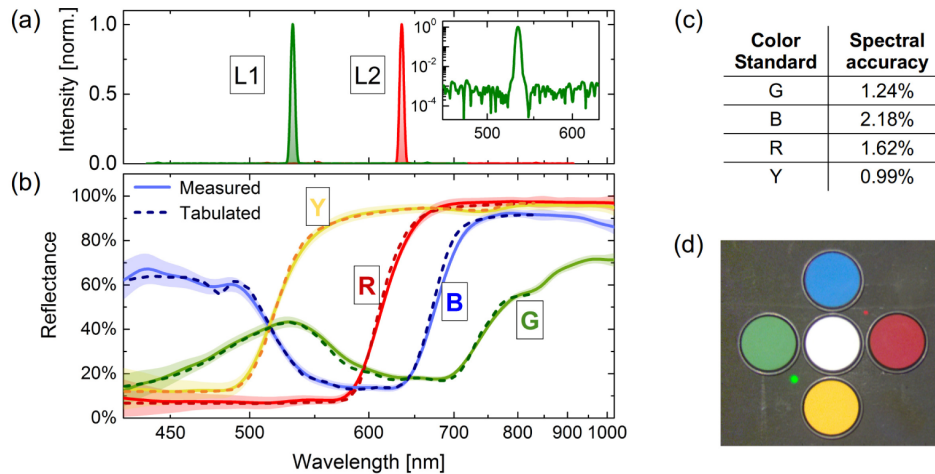


Fig. 4. (a) Measured spectra of lasers L1 and L2 (position scan: ± 5 mm around the ZPD). Inset: spectrum of L1 in log scale. (b) Tabulated (dashed lines) and measured (solid lines) reflectance spectra of the color standards (position scan: ± 1 mm around the ZPD); shaded areas: wavelength-dependent standard deviations of the spectra measured over all points of each color standard surface; (c) spectral accuracy of the hyperspectral image of the color standards; (d) RGB image generated from the hyperspectral data-cube.

We observed that neither the frequency calibration of point (i) nor the retrieved true delay of point (iii) change from day to day; the frequency and phase delay calibration must be repeated only when the alignment of one or more birefringent elements is changed.

3.2. Absolute reflectivity measurements

Figure 4(b) shows the reflectance spectra of the diffusive colorimetric standards, and summarizes the accuracy of the hyperspectral camera in retrieving absolute spectral information. The dashed lines are the certified reflectivity values, while the solid lines are the spectra retrieved from our HSI system and averaged over the surface of each standard. Absolute reflectance was calculated after spectral calibration with the white Spectralon W and correction for spatial and spectral non-uniformities of the illumination by imaging a white Lambertian surface at the object plane (data not shown). The spectral accuracy for each colorimetric sample, estimated as the standard deviation of the difference between measured and certified spectra, is reported in Fig. 4(c). The difference is $<2.18\%$, demonstrating that our camera is able to measure absolute reflectance with very high accuracy in the visible and near-infrared spectral range (400-1000 nm). Figure 4(d) is the color image synthesized from the measured hyperspectral information observed under a D65 illuminant (CIE 1964).

4. Measurement of works of art

Following its performance characterization, we applied our hyperspectral camera to the imaging of artworks. Figure 5 shows the hyperspectral measurement of a fragment from an ancient Egyptian cartonnage dated between Ptolemaic and Roman Periods [37], and currently at the Museo Civico di Crema e del Cremasco (Italy). Also in this case the light source was the 150W Xenon lamp; exposure time was 10ms per image, and we acquired 400 images (± 1 -mm scan). In the field of view, we also placed the white standard for spectral calibration. Figure 5(a) shows the color image generated with the spectral data; the reflectance spectra of three sample pixels are plotted in Fig. 5(c). One of the ancient pigments of the cartonnage is Egyptian Blue ($\text{CaCuSi}_4\text{O}_{10}$), which exhibits unique near-infrared luminescence emission [38]. Thanks to the high throughput of our hyperspectral camera, we could measure the

optical emission of the sample, upon excitation with a broadband LED around $\lambda = 617$ nm and with exposure time of 700ms per image. The measured fluorescence spectrum, shown in Fig. 5(c) as a shaded area, is in excellent agreement with literature [37]. Figure 5(b) shows the image of the intensity of the emission at 900 nm, which reveals the presence of Egyptian Blue in some of the decorations.

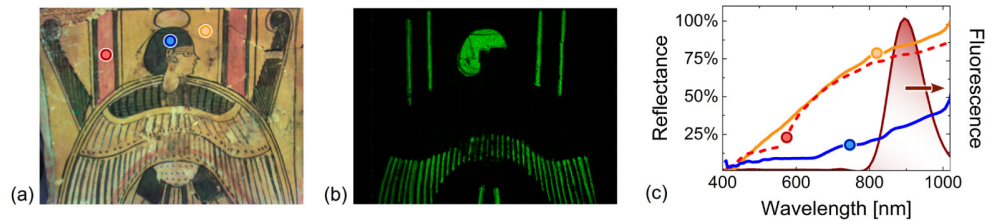


Fig. 5. Hyperspectral imaging of the Egyptian cartonnage (size $\sim 18\text{cm} \times 16\text{cm}$). (a) RGB image synthesized from the hyperspectral data. (b) False-color fluorescence image at $\lambda = 900$ nm after illumination at $\lambda = 617$ nm. (c) Solid/dashed lines: Reflectance spectra of three points of panel (a); shaded area: fluorescence spectrum (the full-resolution RGB and fluorescence images are shown in Visualization 2).

Finally, we demonstrate HSI of a stained glass window, whose plates typically exhibit strong absorption bands located at well-defined wavelengths. Since window glass manufacturing has changed throughout time, spectral characterization is a means to determine the composition of glasses and of their coloring agents, to assess the authenticity of ancient windows [39].

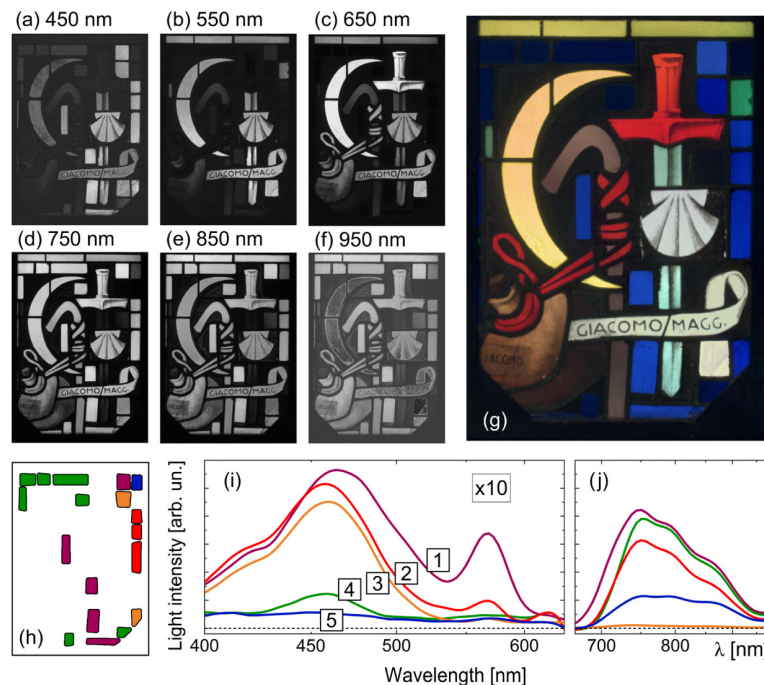


Fig. 6. Hyperspectral imaging of an artistic glass window (A. M. Nardi, 1969). (a-f) Subfigures from the data-cube, at selected wavelengths (the complete spectral data cube as an animation is shown in the associated Visualization 3). (g) Color image synthesized from the spectral data (the full-resolution RGB image is shown in Visualization 4); (h) map and (i,j) corresponding transmitted spectra of the blue tiles, after automatic image segmentation; spectra in the visible range (i) are rescaled by a factor of 10.

Figure 6 shows the results from HSI of a portion of an artistic glass window at Santo Spirito Church in Milan (Italy), designed in 1969 by A. M. Nardi (1897-1973). The window was back-illuminated by natural sunlight, and the camera recorded the transmitted light; exposure time was 100ms per image, and we acquired 400 images (± 1 -mm scan). From the data-cube, we extracted a subset of images at selected wavelengths (Figs. 6(a)–(f)); as expected, each tile absorbs at specific spectral bands. The synthesized RGB color image is shown in Fig. 6(g). We observed that tiles with similar colors exhibit different transmission spectra. Automatic image k -means segmentation of the blue tiles [40] allows their separation into 5 classes with distinct spectral transmission (Figs. 6(h)–(j)) and hence material composition, despite their similar visual appearance. In particular, we identified two blue tiles (cluster 3) with negligible infrared transmission.

5. Conclusions

In conclusion, we have introduced an HSI system using a common-path birefringent interferometer, the TWINS, to perform FT imaging. Our configuration shares the main advantages of FT spectroscopy, such as high light throughput due to the absence of slits, the multiplexing advantage and the user adjustable spectral resolution. The use of the TWINS adds several key advantages: (i) exceptional delay precision and long-term stability; (ii) insensitivity to vibrations, making it suitable for hand-held devices; (iii) low cost and simplicity. We have demonstrated that our compact hyperspectral camera is able to acquire spectral absolute reflectance, transmittance and fluorescence images with broad spectral coverage (400 THz) and high spectral resolution (3 THz), which can be easily increased by the use of thicker birefringent plates. The angular field of view (15.4° , set by the $f = 25$ mm camera lens) can be easily increased by employing camera lenses with shorter focal lengths and using larger plates to avoid vignetting. Thanks to the high interferometric visibility and the throughput offered by our camera the acquisition time of each frame is as short as 10 ms with low-dose illumination by a 150 W Xenon lamp. While our present configuration covers the 400-1000 nm range of silicon detectors, it can be straightforwardly extended to the short-wavelength infrared and mid-infrared ranges using suitable detectors and birefringent materials (such as LiNbO_3 and Hg_2Cl_2), enabling a broad range of imaging and sensing applications.

Appendix: Detection and correction of the delay axis

The FT approach is very sensitive to the exact positioning of the delay line. Deviations from the expected delay may be due to various factors, such as imperfections in the interferometer delay line, or perturbations during the measurement. For this reason, precise measurement of the delay is essential for the correct calculation of the FT. In our camera, the delay can be characterized simply by shining narrowband laser beams on a small area of the scene (e.g. at the edge of the image), and analyzing their interferogram.

The interferogram of a monochromatic light is a pure cosine function. In its general form, it can be written as:

$$y_n = \cos(a \cdot x_n). \quad (3)$$

where a is the cosine angular frequency and x_n is the generic interferometer position at the sampling step n . Conceptually, from the measured interferogram y_n of a monochromatic light it is possible to extract the true interferometer position x_n ; the most straightforward and accurate method is based on the Fourier transform approach. In fact, Eq. (3) can be written as:

$$y_n = \frac{1}{2} e^{i(a \cdot x_n)} + \frac{1}{2} e^{-i(a \cdot x_n)}. \quad (4)$$

By taking the Fourier transform of y_n and then back-transforming only the spectrum at positive frequencies, one isolates the first exponential, obtaining the complex function:

$$\bar{y}_n = \frac{1}{2} e^{i(a \cdot x_n)}. \quad (5)$$

in which the exact interferometer position x_n is proportional to the phase of \bar{y}_n .

We applied this approach to estimate the position deviation of our birefringent interferometer. To this aim, we shone the two narrowband diode laser beams on areas L1 and L2 of the scene. To retrieve the positioning deviation over the broadest excursion of the interferometer, and estimate its effects on the retrieved FT, here we analyze the long interferograms of L1 and L2 obtained after scanning the wedge position ± 5 -mm around the ZPD.

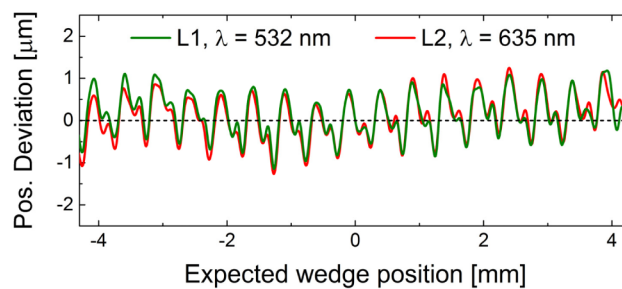


Fig. 7. Deviation of the interferometer delay from its ideal position, deduced from the interferogram of image areas at L1 (green line) and L2 (red line).

Figure 7 shows the deviation of the retrieved position x_n of the interferometer from its expected coordinate, deduced by analyzing independently the interferograms of image areas at L1 (green line) and L2 (red line). The two lines, which are in excellent agreement, show that the deviation is cyclic with remarkably low fluctuations: the maximum excursion is only $\pm 1 \mu\text{m}$, corresponding to 1/40 of the L2 laser optical cycle. Repeated measurements showed reproducible deviations, demonstrating the robustness and reproducibility of our interferometer. The fluctuations can mainly be attributed to imperfections of the delay line and the wedges, while external perturbations are negligible.

The retrieved position x_n can be applied to correct the interferograms during FT data analysis, by means of non-uniform Fourier transform algorithms. To show how positioning deviations affect the calculated spectra, we applied the average of the deviations shown in Fig. 7 for the calculation of the spectra of L1 and L2.

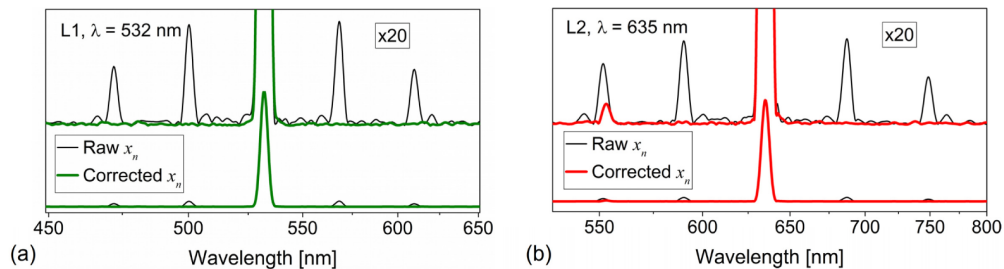


Fig. 8. Spectra of the L1 (a) and L2 (b) lasers. Black lines: FT has been performed taking into account only the expected motor position. Red/green lines: FT has been performed taking into account the measured motor position, which is used to correct the interferogram. The spectra of each panel are also expanded by $20 \times$ for clarity.

The results are shown in Fig. 8. The spectra in black line have been obtained by considering the *expected* motor positioning; the cyclic position deviation results in sidebands, with intensities of 1/20 of the peak. The green and red lines are the spectra obtained after taking into account the average of the *retrieved* positions; in this case, the sidebands are almost completely suppressed, and the background level is at -30dB (see inset of Fig. 4(a)).

Funding

Capes (process CSF-PVE-S-88881.068168/2014-01); Fapemig; CNPq; ERC PoC FLUO (process 825879); Graphene Flagship (785219 GrapheneCore 2).

Acknowledgments

BENF, DCTF, AMdP and CM acknowledge financial support from the Brazilian funding agencies Capes (process CSF-PVE-S-88881.068168/2014-01), Fapemig and CNPq. DP, FP and GC acknowledge financial support from ERC PoC FLUO (process 825879). GC acknowledges financial support from the Graphene Flagship (785219 GrapheneCore 2). Authors wish to thank C. Orsenigo (Università degli studi di Milano), F. Moruzzi and M. Facchi (Museo civico di Crema e del Cremasco), and A. Boni (Comune di Crema) for providing access to the antiquities collection of the late Carla Maria Burri (1935–2009) conserved at the Museo Civico di Crema e del Cremasco.

References

1. W. L. Wolfe, *Introduction to Imaging Spectrometers* (SPIE, 1997).
2. M. T. Eismann, *Hyperspectral Remote Sensing* (SPIE, 2012).
3. H. F. Grahn and P. Geladi, *Techniques and Applications of Hyperspectral Image Analysis* (John Wiley & Sons, 2007).
4. J. M. Amigo, H. Babamoradi, and S. Elcoroaristizabal, "Hyperspectral image analysis. A tutorial," *Anal. Chim. Acta* **896**, 34–51 (2015).
5. E. Ben-Dor, T. Malthus, A. Plaza, and D. Schlapfer, *Airborne Measurements for Environmental Research: Methods and Instruments* (Wiley, 2013), Chap 8.
6. R. G. Sellar and G. D. Boreman, "Classification of imaging spectrometers for remote sensing applications," *Opt. Eng.* **44**(1), 013602 (2005).
7. G. Lu and B. Fei, "Medical hyperspectral imaging: a review," *J. Biomed. Opt.* **19**(1), 010901 (2014).
8. L. M. Dale, A. Thewis, C. Boudry, I. Rotar, P. Dardenne, V. Baeten, and J. A. F. Pierna, "Hyperspectral Imaging Applications in Agriculture and Agro-Food Product Quality and Safety Control: A Review," *Appl. Spectrosc. Rev.* **48**(2), 142–159 (2013).
9. M. Huang, C. He, Q. Zhu, and J. Qin, "Maize seed variety classification using the integration of spectral and image features combined with feature transformation based on hyperspectral imaging," *Appl. Sci. (Basel)* **6**(6), 183 (2016).
10. P. Mouroulis, R. O. Green, and D. W. Wilson, "Optical design of a coastal ocean imaging spectrometer," *Opt. Express* **16**(12), 9087–9096 (2008).
11. R. D. P. M. Scafutto, C. R. de Souza Filho, and B. Rivard, "Characterization of mineral substrates impregnated with crude oils using proximal infrared hyperspectral imaging," *Remote Sens. Environ.* **179**, 116–130 (2016).
12. M. Liu, T. Wang, A. K. Skidmore, and X. Liu, "Heavy metal-induced stress in rice crops detected using multi-temporal Sentinel-2 satellite images," *Sci. Total Environ.* **637-638**, 18–29 (2018).
13. H. Liang, "Advances in multispectral and hyperspectral imaging for archaeology and art conservation," *Appl. Phys., A Mater. Sci. Process.* **106**(2), 309–323 (2012).
14. C. Fischer and I. Kakoulli, "Multispectral and hyperspectral imaging technologies in conservation: current research and potential applications," *Stud. Conserv.* **51**, 3–16 (2006).
15. C. Cucci, J. K. Delaney, and M. Picollo, "Reflectance Hyperspectral Imaging for Investigation of Works of Art: Old Master Paintings and Illuminated Manuscripts," *Acc. Chem. Res.* **49**(10), 2070–2079 (2016).
16. N. A. Hagen and M. W. Kudenov, "Review of snapshot spectral imaging technologies," *Opt. Eng.* **52**(9), 090901 (2013).
17. N. Gat, "Imaging spectroscopy using tunable filters: a review," *Proc. SPIE* **4056**, 50–64 (2000).
18. S. P. Davis, M. C. Abrams, and J. W. Brault, *Fourier Transform Spectrometry* (Elsevier, 2001).
19. P. B. Fellgett, "On the ultimate sensitivity and practical performance of radiation detectors," *J. Opt. Soc. Am.* **39**(11), 970–976 (1949).
20. P. Jacquinet, "New developments in interference spectroscopy," *Rep. Prog. Phys.* **23**(1), 267–312 (1960).
21. A. P. Fossi, Y. Ferrec, N. Roux, O. D'almeida, N. Guerinéau, and H. Sauer, "Miniature and cooled hyperspectral camera for outdoor surveillance applications in the mid-infrared," *Opt. Lett.* **41**(9), 1901–1904 (2016).

22. M. J. Persky, "A review of spaceborne infrared Fourier transform spectrometers for remote sensing," *Rev. Sci. Instrum.* **66**(10), 4763–4797 (1995).
23. A. Hegyi and J. Martini, "Hyperspectral imaging with a liquid crystal polarization interferometer," *Opt. Express* **23**(22), 28742–28754 (2015).
24. I. August, Y. Oiknine, M. AbuLeil, I. Abdulhalim, and A. Stern, "Miniature Compressive Ultra-spectral Imaging System Utilizing a Single Liquid Crystal Phase Retarder," *Sci. Rep.* **6**(1), 23524 (2016).
25. A. Jullien, R. Pascal, U. Bortolozzo, N. Forget, and S. Residori, "High-resolution hyperspectral imaging with cascaded liquid crystal cells," *Optica* **4**(4), 400–405 (2017).
26. M. Françon and S. Mallick, *Polarization Interferometers Applications in Microscopy and Macroscopy* (Wiley-Interscience, 1972).
27. A. Harvey and D. Fletcher-Holmes, "Birefringent Fourier-transform imaging spectrometer," *Opt. Express* **12**(22), 5368–5374 (2004).
28. C. Bai, J. Li, Y. Xu, H. Yuan, and J. Liu, "Compact birefringent interferometer for Fourier transform hyperspectral imaging," *Opt. Express* **26**(2), 1703–1725 (2018).
29. T. Mu, C. Zhang, Q. Li, L. Zhang, Y. Wei, and Q. Chen, "Achromatic Savart polariscope: choice of materials," *Opt. Express* **22**(5), 5043–5051 (2014).
30. D. Brida, C. Manzoni, and G. Cerullo, "Phase-locked pulses for two-dimensional spectroscopy by a birefringent delay line," *Opt. Lett.* **37**(15), 3027–3029 (2012).
31. C. A. Manzoni, D. Brida, and G. N. F. Cerullo, US Patent: 9182284 (2015).
32. A. Oriana, J. Réhault, F. Preda, D. Polli, and G. Cerullo, "Scanning Fourier transform spectrometer in the visible range based on birefringent wedges," *J. Opt. Soc. Am. A* **33**(7), 1415–1420 (2016).
33. A. Perri, F. Preda, C. D'Andrea, E. Thyraug, G. Cerullo, D. Polli, and J. Hauer, "Excitation-emission Fourier-transform spectroscopy based on a birefringent interferometer," *Opt. Express* **25**(12), A483–A490 (2017).
34. J. Réhault, R. Borrego-Varillas, A. Oriana, C. Manzoni, C. P. Hauri, J. Helbing, and G. Cerullo, "Fourier transform spectroscopy in the vibrational fingerprint region with a birefringent interferometer," *Opt. Express* **25**(4), 4403–4413 (2017).
35. J. Réhault, M. Maiuri, C. Manzoni, D. Brida, J. Helbing, and G. Cerullo, "2D IR spectroscopy with phase-locked pulse pairs from a birefringent delay line," *Opt. Express* **22**(8), 9063–9072 (2014).
36. V. Saptari, *Fourier Transform Spectroscopy Instrumentation Engineering* (SPIE, 2004).
37. D. Comelli, V. Capogrosso, C. Orsenigo, and A. Nevin, "Dual wavelength excitation for the time-resolved photoluminescence imaging of painted ancient Egyptian objects," *Herit. Sci.* **4**(1), 21 (2016).
38. G. Accorsi, G. Verri, M. Bolognesi, N. Armaroli, C. Clementi, C. Miliari, and A. Romani, "The exceptional near-infrared luminescence properties of cuprorivaite (Egyptian blue)," *Chem. Commun. (Camb.)* **23**(23), 3392–3394 (2009).
39. W. Meulebroeck, H. Wouters, K. Nys, and H. Thienpont, "Authenticity screening of stained glass windows using optical spectroscopy," *Sci. Rep.* **6**(1), 37726 (2016).
40. A. K. Jain and R. C. Dubes, *Algorithms for Clustering Data* (Prentice-Hall, 1988).